ACS APPLIED MATERIALS & INTERFACES

www.acsami.org

Research Article

Nanoscale Adhesion and Material Transfer at 2D MoS_2–MoS_2 Interfaces Elucidated by In Situ Transmission Electron Microscopy and Atomistic Simulations

Sathwik Reddy Toom, Takaaki Sato, Zachary Milne, Rodrigo A. Bernal, Yeau-Ren Jeng, Christopher Muratore, Nicholas R. Glavin, Robert W. Carpick, and J. David Schall*

Cite This: *ACS Appl. Mater. Interfaces* 2024, 16, 30506–30520

Read Online

ACCESS | Metrics & More | Article Recommendations | Supporting Information

ABSTRACT: Low-dimensional materials, such as MoS_2, hold promise for use in a host of emerging applications, including flexible, wearable sensors due to their unique electrical, thermal, optical, mechanical, and tribological properties. The implementation of such devices requires an understanding of adhesive phenomena at the interfaces between these materials. Here, we describe combined nanoscale *in situ* transmission electron microscopy (TEM)/atomic force microscopy (AFM) experiments and simulations measuring the work of adhesion (W_{adh}) between self-mated contacts of ultrathin nominally amorphous and nanocrystalline MoS_2 films deposited on Si scanning probe tips. A customized TEM/AFM nanoindenter permitted high-resolution imaging and force measurements *in situ*. The W_{adh} values for nanocrystalline and nominally amorphous MoS_2 were 604 ± 323 mJ/m^2 and 932 ± 647 mJ/m^2, respectively, significantly higher than previously reported values for mechanically exfoliated MoS_2 single crystals. Closely matched molecular dynamics (MD) simulations show that these high values can be explained by bonding between the opposing surfaces at defects such as grain boundaries. Simulations show that as grain size decreases, the number of bonds formed, the W_{adh} and its variability all increase, further supporting that interfacial covalent bond formation causes high adhesion. In some cases, sliding between delaminated MoS_2 flakes during separation is observed, which further increases the W_{adh} and the range of adhesive interaction. These results indicate that for low adhesion, the MoS_2 grains should be large relative to the contact area to limit the opportunity for bonding, whereas small grains may be beneficial, where high adhesion is needed to prevent device delamination in flexible systems.

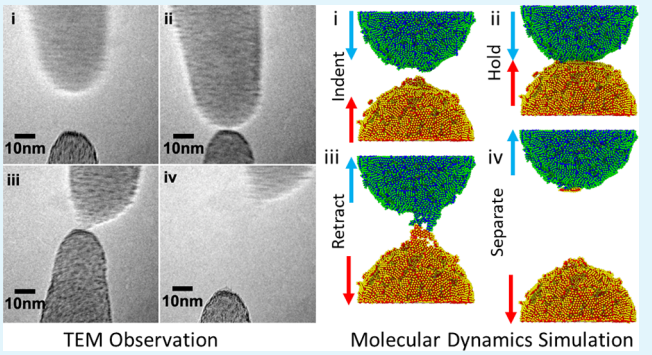

KEYWORDS: *molybdenum disulfide, work of adhesion, material transfer, in situ transmission electron microscopy (TEM), molecular dynamics simulations (MD)*

INTRODUCTION

Recently, interest has rapidly grown in manufacturing flexible electronics, which can bend, twist fold, and wrap over the supporting surfaces without transfer of material or other changes in their properties and characteristics.[1,2] Flexible electronic devices have a wide range of applications in health care (skin, implantable devices, wearable cardiovascular devices, etc.),[3,4] communication and sensing,[5] and solar cells,[6] among others. Low-dimensional materials, including graphene, boron nitride, gallium nitride, and transition metal dichalcogenides (TMDs) like MoS_2 and WS_2, and heterostructures that combine them lead a revolution in flexible electronics due to their unique structure and remarkable chemical, optical, thermal, and electromechanical properties.[7,8] These materials may serve as the flexible substrate for the electronic components in flexible devices or as the devices themselves. Molybdenum disulfide (MoS_2) is particularly promising in device applications. Next to graphene, MoS_2 is one of the most widely used and important 2D materials, finding applications in areas including semiconductors,[9,10] lubrication,[11] clean energy,[12] hydrogen detection,[13] and biosensing.[14]

However, many challenges remain,[15] including understanding the response of electronic properties to bending and stretching strains and to interlayer adhesion. Interlayer adhesion is especially important when MoS_2 will be used as a release layer in flexible electronics.[7,16,17] While many have examined the electronic properties of these materials, including their strain

Received: February 26, 2024
Revised: May 8, 2024
Accepted: May 10, 2024
Published: May 28, 2024

https://doi.org/10.1021/acsami.4c03208
ACS Appl. Mater. Interfaces 2024, 16, 30506–30520

dependence,[2,18,19] fewer have studied adhesion. Understanding the adhesive properties of vdW materials is still lacking, especially at sub-100 nm scales, where the most novel physical effects occur. Fundamental studies of these materials' adhesion mechanics are needed since the growth, processing, and function of device applications all hinge crucially on the adhesive and mechanical properties, particularly at high strains.

Notably, factors affecting interlayer adhesion energy (the thermodynamic free energy per unit area to separate two layers, e.g., through fraction or cleavage; also referred to as the work of cohesion) and their adhesion to substrates or other materials (the work of adhesion, W_{adh}) are not well understood but are crucial for developing flexible electronics. W_{adh} is a critical parameter used to describe adhesive contacts.[20] For dissimilar materials or misoriented surfaces of the same type of material, W_{adh} is expressed using Dupre's relation $W_{adh} = \gamma_1 + \gamma_2 + \gamma_{12}$, where γ_1 and γ_2 are the two surface energies per unit area and γ_{12} is the interfacial energy per unit area. Most prior adhesion research studies have focused on two classes of MoS_2: polycrystalline coatings for tribological applications and mechanically exfoliated MoS_2 crystals on various substrates and in heterostructures. MoS_2 is used widely as a lubricant additive and as a solid lubricant coating. Strong adhesion between the coating and the substrate contributes to the lasting lubricant performance. In most solid lubrication applications, the MoS_2 coating is deposited onto a substrate via sputtering or similar processes. Substrate adhesion has been studied for these systems.[21−24] Notably, Fleischauer and co-workers investigated sputter-deposited MoS_2 and found that lower porosity and higher purity resulted in lower adhesion.[22] Furthermore, applied stress reoriented crystallites and induced further crystallization. However, none of these directly address adhesion between layers within MoS_2 films themselves (i.e., cohesion).

Adhesion between mechanically exfoliated MoS_2 single-crystal flakes and various substrates (including MoS_2 itself) has been measured.[25−28] Only a few experiments report W_{adh} values for self-mated MoS_2, and values vary widely. Lloyd et al. used a blister test, finding $W_{adh} = 42 \pm 20$ mJ/m^2.[26] Rokni and Lu measured adhesion between mechanically exfoliated MoS_2 and a MoS_2 nanomesa glued to a flattened atomic force microscopy (AFM) tip, reporting $W_{adh} = 482 \pm 32$ mJ/m^2.[25] Tang et al. utilized a scanning tunneling microscope (STM) with a transmission electron microscope to measure adhesion. The STM tip was oriented parallel to the MoS_2 planes, which was then wedged between the layers to peel apart the MoS_2 along the basal plane.[28] They calculated $\gamma_1 = 110$ mJ/m^2, which corresponds to $W_{adh} = 220$ mJ/m^2. Fang et al. employed a peel-to-fracture method combined with a continuum model, finding $W_{adh} = 550 \pm 13$ mJ/m^2.[29] Using density functional theory, they obtained $W_{adh} = 422$ mJ/m^2.[30] Several others have calculated W_{adh} values using theoretical approaches. Weiss and Phillips first calculated the $W_{adh} = 490 \pm 40$ mJ/m^2 using a Lennard-Jones potential.[30] Employing *ab initio* total energy calculations, Fuhr et al. calculated $W_{adh} = 560$ mJ/m^2.[31] Using more accurate random phase approximation (RPA) methods, Björkman et al. showed that almost universally 2D materials (*e.g.*, graphene, MoS_2, h-BN, and others) have exfoliation energies, which are equivalent to W_{adh} of 320 mJ/m^2.[32]

This wide range of literature values may be attributed to differences in surface conditions (*e.g.*, roughness, adsorbed species including water, internal defects, and chemical reactivity between the surfaces). As the experiments all rely on mechanically exfoliated MoS_2 single crystals, the effects of step edges and grain boundaries are typically neglected, although other internal crystal defects like dislocations, vacancies, and impurities may be present. We are unaware of any measurements of the work of adhesion between polycrystalline MoS_2 films.

Here, we present results from nanoscale adhesion experiments between AFM tips coated with nominally amorphous and nanocrystalline 2D MoS_2 films that are a few layers (2−5 nm) thick. These experiments employ a customized *in situ* transmission electron microscopy (TEM)/AFM nanoindenter to measure W_{adh} while viewing the tip-to-tip contact in real time to observe any related changes in the MoS_2 films. The W_{adh} measured is significantly higher than the previous literature values. Closely matched MD simulations were used to provide atomic-level understanding of the interfacial chemistry effects occurring in the experiments, which affect W_{adh}. From this, we demonstrate that W_{adh} depends on the MoS_2 structure and grain size due to the formation of covalent bonds across the interface at defect sites.

RESULTS AND DISCUSSION

Experimental Measurement of Adhesion. To study the contact and adhesion behavior of MoS_2 at the nanoscale, we made use of an *in situ* TEM nanoindenter (Oxford/Hysitron PI-95) modified to allow two AFM tips to come into contact with one another. A more complete description of the TEM/AFM nanoindenter along with a description of the sample preparation procedure is provided in the Methods section. Si AFM cantilevers with integrated tips were sputter-coated with an ultrathin film of MoS_2 at either room temperature (22 °C) or elevated temperature (400 °C), as described in the Methods section. Previous work has shown that films deposited at room temperature are largely amorphous, with a small degree of isolated crystallization and layering.[33] Deposition at elevated temperatures promotes thermal annealing and crystallization in the MoS_2 film and reduces the amount of amorphous character.[33−35] Raman and high-resolution TEM (HRTEM) were used to confirm the structure of films after deposition on the AFM probe tips.

Raman spectra for the films deposited at 22 and 400 °C were acquired using a Renishaw in Via Raman microscope with a 20 mW 514 nm excitation laser power and a grating size of 1800 lines/mm with 30 s acquisition time. The spectra in the region of the E_{2g} and A_{1g} peaks are presented in Figure 1. The peak positions ($E_{2g} = 380$ cm^{-1} and $A_{1g} = 405$ cm^{-1}) of the MoS_2 film deposited at 400 °C are in good agreement with those reported for bulk MoS_2 ($E_{2g} = 383$ cm^{-1} and $A_{1g} = 409$ cm^{-1}).[36] The presence of these peaks is consistent with the presence of nanocrystalline MoS_2. The spectrum for the film deposited at 22 °C is largely featureless with the exception of a small bump in the vicinity of the expected A_{1g} peak. This finding is consistent with a nominally amorphous film with a low degree of crystallinity. Note that the laser spot is focused in the area of the tip, but the laser spot size is 10 μm, so the Raman spectra include the probe tip and cantilever base as illustrated schematically in Figure 1. HRTEM was used to confirm that the structures at the apex of the tip and along the wider flank of the tip were consistent with one another (see Figures S1 and S2 and additional discussion provided in the Supporting Information). As such, the Raman results, though covering a wider area, can be assumed to be representative of MoS_2 near the apex of the tip.

Figure 2 shows that the TEM image of a Si probe pairs with the MoS_2 deposited at 22 °C coating [Figure 2a,b, tip pair 1] and

https://doi.org/10.1021/acsami.4c03208
ACS Appl. Mater. Interfaces 2024, 16, 30506−30520

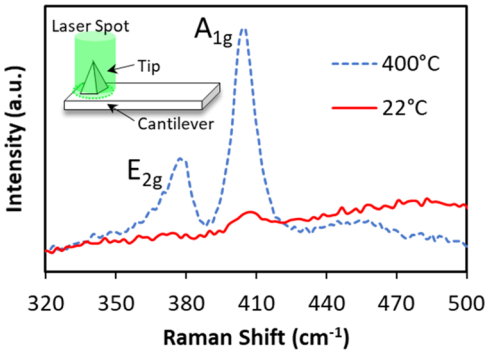

Figure 1. Raman spectra for the MoS_2 films deposited at 22 °C (solid red line) and 400 °C (dashed blue line) shown in the vicinity of the E_{2g} and A_{1g} Raman peaks. The laser probe is focused in the area of the probe tip, but due to the spot size, the spectra are gathered for the tip and part of the flat region of the cantilever as illustrated schematically in the inset diagram. Raman spectra were acquired using a Renishaw in Via Raman microscope with a 20 mW 514 nm excitation laser power and a grating size of 1800 lines/mm with 30 s acquisition time.

MoS_2 coatings deposited at 400 °C [Figure 2c,d, tip pair 2]. The "lower" and "upper" tips are referenced with respect to the experimental setup discussed in the Methods section. Additional TEM images of the films are provided in Figures S3 and S4 in the Supporting Materials. While layering is present in some regions of the films deposited at 22 °C, those layered regions appear to be oriented randomly relative to the surface of the tip. This film thus contains some nanocrystallites, but there are fewer of them as compared with the film deposited at 400 °C. This finding is consistent with the assertion that a small bump near the expected A_{1g} peak observed in the Raman spectrum for the film deposited at 22 °C is related to a small amount of crystallinity in an otherwise amorphous material (red line, Figure 1). In contrast, for the film deposited at 400 °C, the layers are oriented parallel to the underlying surface of the tip, as seen in Figure 2c,d (and additional images provided in Figure S3 in the Supporting Information). Note that layers will only be resolved when the plane of the layers in a local region is aligned with the TEM beam direction; thus, due to the high degree of curvature of the tip, including local irregularities and the random orientation of the crystal layers, layering may be present even if not resolved in the TEM image.

MoS_2 films deposited on different probes with the same deposition parameters (either 22 or 400 °C) were analyzed by high-resolution TEM. Three to eight layers of MoS_2 are seen uniformly coating the Si tips coated at 400 °C. The coatings are approximately 2−5 nm thick. The separation between the layers is 0.63 ± 0.10 nm, which agrees reasonably well with the known layer spacing of MoS_2 of 0.62 nm.[37] The interatomic spacing was measured using the intervals of dark and white contrast along the in-plane direction, as illustrated in Figure 3a (additional images in Figure S3 in the Supporting Information). For reference, the literature values for the lattice spacings are illustrated schematically in the atomic snapshot provided in Figure 3b.[37] The spacing 0.28 ± 0.04 nm matches the expected spacing of 0.27 nm between rows of S (or Mo) atoms when viewed along the "zigzag" or the $\langle 11\bar{2}0 \rangle$ direction. This occurs at certain locations where, by chance, a crystalline grain happens to be oriented with its crystal axis sufficiently close to the electron beam's direction. Terminations of layers apparently due to the nanocrystalline grain structure of MoS_2 are seen in the red circled area in Figure 3a. All aspects of the TEM observations confirm the expected

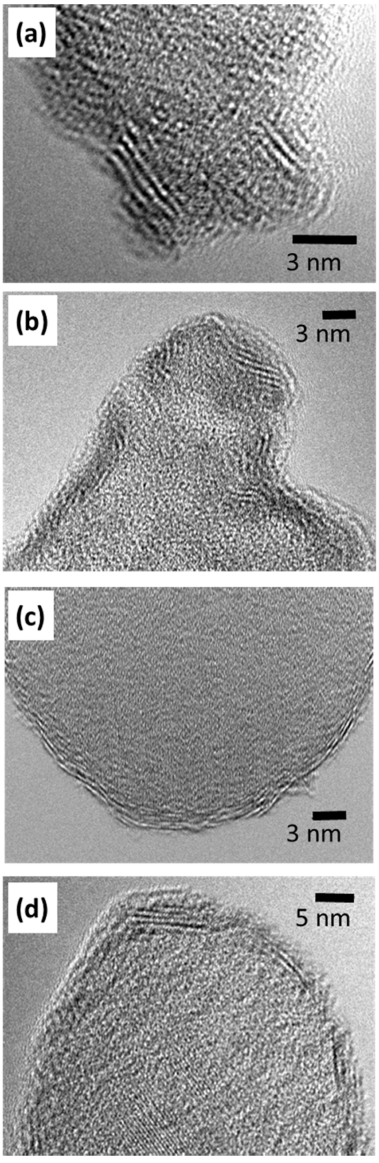

Figure 2. TEM views the MoS_2-coated scanning probe tips of (a) the upper fixed cantilever and (b) lower fixed cantilever with the MoS_2 film deposited at 22 °C coating, which we refer to as "tip pair 1", and (c) the upper fixed cantilever and (d) lower fixed cantilever with the MoS_2 film deposited at 400 °C, which we refer to as "tip pair 2".

presence of nanocrystalline MoS_2 on the film deposited at 400 °C, whereas the film deposited at 22 °C can be considered nominally amorphous.

After this initial characterization of the tips, a series of contact separation tests were carried out, in which the tip pairs shown in Figure 2 were brought in and out of contact four times. The tips, initially out of contact, are brought together by advancing the indenter using a piezoelectric actuator. Eventually, pull-in (also known as snap-to-contact) occurs, which corresponds to the attractive force gradient exceeding the spring constant of the cantilever.[38] The pull-in distance (*i.e.*, the change in the tip-to-tip separation distance from just before to just after pull-in) is determined from subsequent image analysis. Care was taken to ensure that the maximum load reached during contact was held at a value of 0 nN, *i.e.*, no net positive external load was applied. Thus, the tips were held together only by their adhesion force before the separation process was initiated until pull-off occurs.

https://doi.org/10.1021/acsami.4c03208
ACS Appl. Mater. Interfaces 2024, 16, 30506−30520

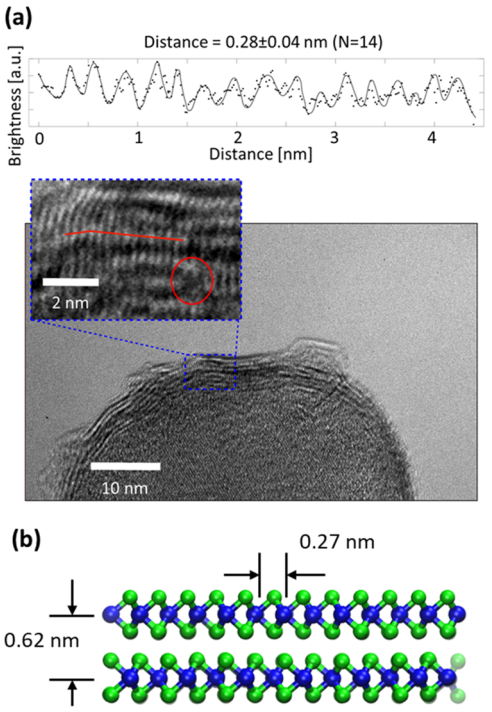

Figure 3. (a) HRTEM image of a Si probe with a nanocrystalline MoS_2 coating (400 °C deposition temperature). The inset shows an atomic spacing that corresponds to the atomic spacing of S (or Mo) when viewed along the zigzag direction of the MoS_2. Lattice spacing was measured using the intervals of light−dark contrast along the red line shown in the inset. The red circle shows the termination of an MoS_2 layer. (b) Atomistic representation of the MoS_2 structure as viewed looking down the zigzag $\langle 11\bar{2}0 \rangle$ direction, showing atomic spacings reported by Winer.[37]

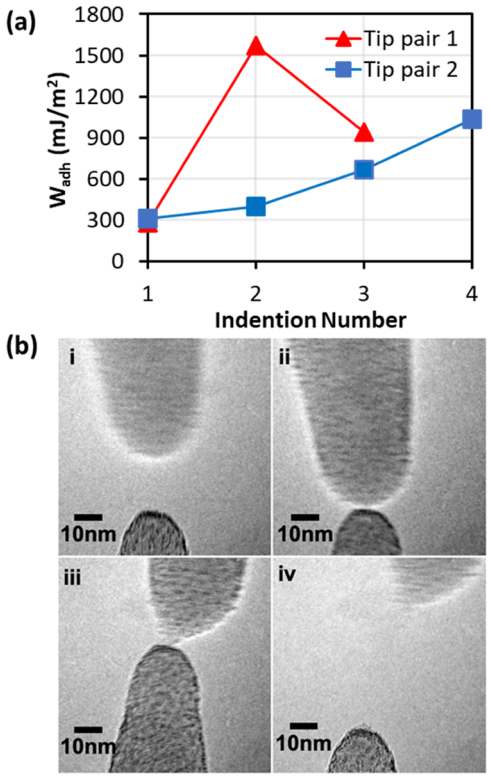

Figure 4. (a) Work of adhesion for tip pair 1 (deposited at 22 °C, red triangles) and for tip pair 2 (deposited at 400 °C, blue squares) and (b) *in situ* TEM images for tip pair 2 (i) just before snap-in, (ii) after snap-in, (iii) just before separation, and (iv) just after separation. Just before separation, a bridge or neck of the material is observed between the opposing tips. After separation, some material appears to have transferred between the tips. A movie of the entire contact experiment is provided in Video 2 in the Supporting Materials.

The tips were also carefully aligned such that contact was made between the apex of the opposing tip pairs in the focal plane. The pull-off distance (*i.e.*, the change in the tip-to-tip separation distance from just before to just after pull-off) is determined from subsequent image analysis. Video 1 provided in the Supporting Information shows the first contact between tip pair 1. Video 2 shows the first contact between tip pair 2. The videos show that there is a minimal overlap between the probes while in contact, suggesting that the tips are well aligned in the focal plane. Misalignment of the probes would introduce shear during contact, though based on simulations of contact between offset probes (see the Supporting Information), the contribution of shear to the forces felt by the tip is expected to be small.

The work of adhesion was then calculated for each tip pair (Figure 4a). In this work, the Snap-in/pull-off Numerical Adhesion Parameter method (or SNAP method) was used to calculate the W_{adh}.[38] In the SNAP method, a fitting routine is employed to find the best fit values of work of adhesion from the pull-in distance (which is converted to the pull-in force using k_n), the pull-off distance (which is converted to the pull-off force), and the shape of the tips obtained from TEM images. The formulas originally derived by Jacobs et al.[38] for a tip on a flat substrate were modified to use in tip-on-tip calculations. The code was modified to calculate one effective tip shape by taking the difference between the two tips, the lower tip and the upper tip. The improved feature allows to calculate W_{adh} of a tip-on-tip system. A copy of the modified code is available via GitHub.[39]

The W_{adh} for the amorphous MoS_2 (tip pair 1) varies substantially (Figure 4a, red triangles) while the nanocrystalline MoS_2 (tip pair 2) shows a consistent increase in W_{adh} with repeated contacts (Figure 4a, blue squares). Due to the small sample size, it is difficult to draw any reliable conclusions regarding the trends shown in Figure 4a; however, one thing is clear, and that is that the adhesion is generally greater than what has been measured previously for single-crystal mechanically exfoliated MoS_2. The average W_{adh} values are 932 ± 647 and 604 ± 323 mJ/m^2 for tip pair 1 and tip pair 2, respectively. Between indention numbers 3 and 4, the upper tip in tip pair 1 broke, possibly due to the high pull-off forces encountered during separation so this data point was excluded. Only the lowest W_{adh} values from the tip-on-tip experiments described here (indention number 1 for both tip pairs) are in reasonable agreement with the value reported by Rokni and Lu,[25] which is on the higher end of values reported in the literature. The remaining runs greatly exceed the reported literature values for W_{adh}. The theoretical value for the work of cohesion of crystalline MoS_2 (the energy per unit area to cleave bulk MoS_2) purely from van der Waals forces is 320 mJ/m^2.[32] Figure 4b shows the evolution of the contact via *in situ* TEM images for tip pair 2. In this sequence, the upper fixed probe tip is moved toward the lower probe tip [Figure 4(b-i) and (b-ii)]. Then, as the upper tip is pulled away, necking of MoS_2 is observed Figure 4(b-iii). After separation, material transfer can be observed, as illustrated by the distortion of the upper tip relative to the original shape [Figures 4(b-iv) and 2d]. High adhesion forces and the transfer of material suggest mechanisms at work in

https://doi.org/10.1021/acsami.4c03208
ACS Appl. Mater. Interfaces 2024, 16, 30506−30520

addition to van der Waals dispersion forces between MoS_2 layers.

Molecular Dynamics Simulation of Adhesion. To elucidate and identify these mechanisms, we implemented an MD scheme that closely matches the experimental geometry and structure of the tips and the MoS_2 films. To investigate the effect of the MoS_2 film structure on adhesion, four tip probe pairs were generated. Each probe pair starts with an opposing pair of 5 nm radius hemispherical Si base probes, to which a three-layer thick MoS_2 film is added. Only the grain size of the nanocrystalline film on each probe pair is varied from 1.1 to 4.4 nm. In what follows grain sizes of 1.1, 1.5, 2.0, and 4.4 nm and are referred to as Tiny, Small, Medium, and Large, respectively. The resulting probes all have an outer radius of approximately 7 nm, which is approximately the same size as experimental tip pair 1. Details regarding the construction of the starting coordinates are given below in the Methods section.

In an effort to validate the structure of the model MoS_2 films with respect to the experimental structure, the combined phonon density of states (PDOS) was calculated for each tip. The PDOS is a measure of the intensity of vibrational modes of atoms in a material and allows direct comparison to other spectroscopic methods, such as Raman.[40] The method used to calculate the PDOS was previously given in Rouhani et al.[41] and is briefly described again below in the Methods section. The PDOS for bulk MoS_2 from Rouhani et al. has been replotted in the upper panel in Figure 5. To ease comparison with the

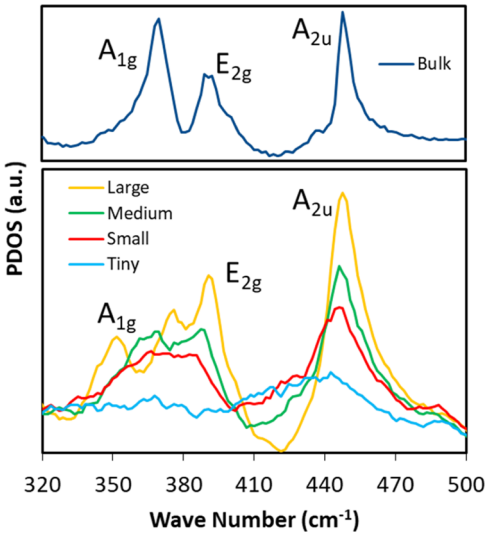

Figure 5. Simulated phonon density of states (PDOS) for the tiny, small, medium, and large grain sizes in the region containing the A_{1g}, E_{2g}, and A_{2u} peaks. The simulated PDOS for bulk 2H-MoS_2 is included for reference. Tiny, small, medium, and large correspond to MoS_2 grain sizes of 1.1, 1.5, 2.0, and 4.4 nm, respectively.

experiment, the PDOS is plotted over the same range of wave numbers as the Raman data presented in Figure 1. The three peaks were identified from the contributions of the partial PDOS for Mo and S to the total PDOS as described previously by Rouhani et al.[41] The peaks from left to right are A_{1g}, E_{2g}, and A_{2u} at 369, 393, and 449 cm^{-1}, respectively. The PDOS calculation statistically samples all thermally active vibrational modes statistically. The A_{2u} mode found at 449 cm^{-1} in PDOS is not Raman active and does not appear in the experimental Raman spectra (Figure 1). The peak positions and peak order do not match the reported experimental positions and order (E_{2g} = 383 cm^{-1}, A_{1g} = 409 cm^{-1}, and A_{2u} = 470 cm^{-1}).[36] The empirically based interatomic potential used to describe the MoS_2 interaction in the MD simulation was not specifically fit to reproduce vibrational modes, so the failure to match the experimental peak position and peak order is not surprising. Nonetheless, the calculated PDOS serves as a qualitative guide for comparison. Note that the ratio of A_{1g} to E_{2g} PDOS peak intensities for the bulk MoS_2 does closely match that of the nanocrystalline film deposited at 400 °C (Figure 1, blue line) and bulk MoS_2.[36]

The simulated PDOS spectra for each of the four simulated tip probes are plotted in the lower panel of Figure 5. At the smallest grain size (tiny = 1.1 nm, light blue line), the PDOS is almost featureless with only a small bump in the vicinity of the A_{2u} peak. As the grain size increases, the peak intensity increases and the individual peaks become more distinct. This can be understood through the following argument: as grain size increases, the ratio of grain area to grain boundary increases, leading to more ordered films. At the smallest grain size, the structure is dominated by grain boundaries and the system is highly disordered due to misorientation of the individual grains. This compares well with the experimental Raman data presented in Figure 1 and strengthens the argument that the simulated films represent a reasonable approximation of the film structures of the nominally amorphous and nanocrystalline films deposited on the AFM probe tips.

Representative force displacement curves for each system are plotted in Figure 6a–c and videos of these MD simulations are provided in the Supporting Information. Videos 3–6 correspond to the tiny, small, medium, and large grain sizes, respectively. In each case, the tip pairs are loaded until a target load of 10 nN is met or exceeded. The load is then held at a constant 10 nN for 25 ps before the upper tip is retracted (full details are provided below in the Methodssection). Due to the sampling rate in the loading algorithm, the actual load may overshoot the target load for a short time before returning to 10 nN during the holding phase. This brief transient is not expected to affect the resulting adhesion significantly. In the experiments, the tips are held in contact with an average force of 0 nN. This condition is difficult to achieve in the simulations due to limitations with the simulation software.

The tip pairs with small and large grain sizes (see Figure 6c) exhibit minimal hysteresis during the indent-hold-retract (IHR) cycle, which suggests that the contact process is nearly fully reversable. The tip–tip pairs with tiny and medium grain sizes show significant hysteresis. In the medium case (Figure 6b), the force during retraction remains negative over an extended range (over 2 nm separation distance) relative to the others. To investigate repeatability, each tip–tip pair was run six times using six different random number seeds to set the initial Gaussian distribution of atomic velocities. All other simulation parameters were unchanged. The average W_{adh} for each grain size is shown in Figure 6d. The error bars represent the standard deviations of the six trial runs. The W_{adh} was estimated using the Derjaguin–Müller–Toporov (DMT)[52,53] approximation for hard spherical contacts as

$$W_{adh} = \frac{F_{pull-off}}{2\pi R} \quad (1)$$

where $F_{pull\text{-}off}$ is the maximum tensile force (*i.e.*, the negative-most force on the curves shown in Figure 6a) required to

https://doi.org/10.1021/acsami.4c03208
ACS Appl. Mater. Interfaces 2024, 16, 30506–30520

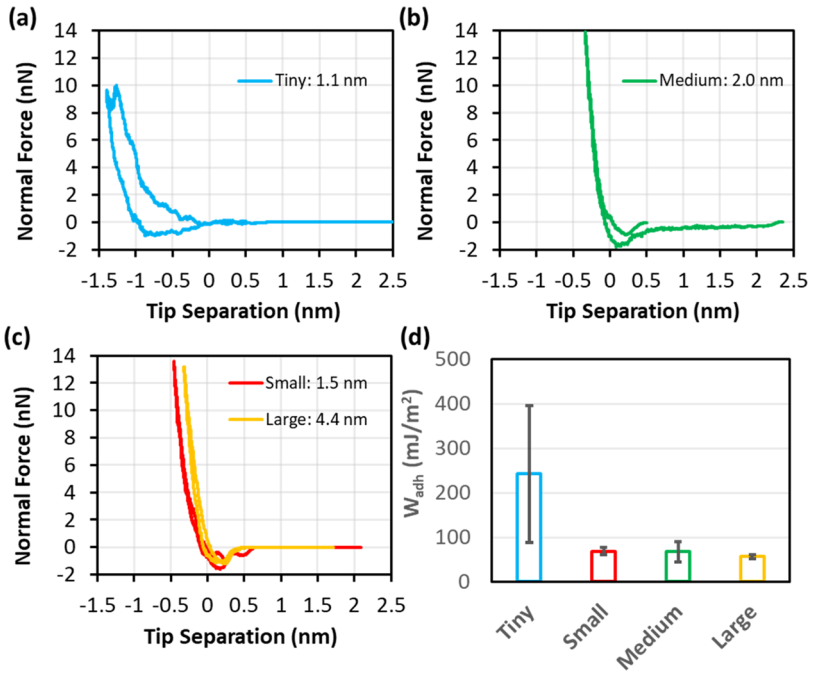

Figure 6. (a) Representative force−separation curves for tiny (1.1 nm), (b) medium (2.0 nm) (c) small (1.5 nm) and large (4.4 nm) MoS2 grain sizes. (d) Average W_{adh}. The error bars indicate the standard deviation for six different randomized starting conditions.

separate the two surfaces, and R is the composite radius of the probe tip pair, which is given as

$$\frac{1}{R} = \frac{1}{R_1} + \frac{1}{R_2} \tag{2}$$

Here, R_1 and R_2 are the respective radii of the tips in the contacting pair. Using the outer radii of the coated tips, the effective tip radius, R, is then calculated to be 3.52 nm. The DMT model assumes a homogeneous tip material (*i.e.*, no coating) that is effectively rigid. Thus, it does not account for the nonuniform composition, nor any elastic or plastic deformation of the materials. However, it does provide a useful benchmark for comparing different tip pairs and comparing to the literature, where the same formula is often used. Moreover, for cases where only elastic deformation occurs, it provides a reasonable estimate for W_{adh} based on our calculations for the effect of elastic deformation and for the presence of the coating,[42] particularly when Tabor's parameter (the ratio of the elastic deformation caused by adhesion to the spatial range of adhesive forces) is small.[43,44] Tabor's parameter is estimated in the Supporting Information and is indeed confirmed to be sufficiently low that the DMT model is reasonable to use.

The average W_{adh} values for small, medium, and large grain size systems all fall within one standard deviation of one another. The combined average W_{adh} for small, medium, and large grain size systems is 64 ± 14 mJ/m^2, which falls close to a lower range of experimentally reported W_{adh} values, i.e., that reported by Lloyd,[26] but lower than the majority of the reported literature values.[25,28,29] These values are also lower than the W_{adh} for bulk single-crystal MoS_2 (248 mJ/m^2) calculated using the Stewart−Spearot reactive empirical bond-order potential[45] used in this work to describe the MoS_2 interactions. The relatively low values found in the tip-on-tip adhesion simulations are explained in part by tip registry effects. In the bulk crystal, the atomic lattices are perfectly aligned. The intimate contact between the aligned layers enhances the adhesion. We found the work of adhesion for misaligned lattice drops to 168 mJ/m^2. See the Supporting Materials for further details on the calculation of the W_{adh} for bulk MoS_2. Additional factors included defects, grain boundaries, and faceting (flattening) of the MoS_2 structure at the apex of the tip, which all reduce the true contact area and hence the W_{adh}.

The average W_{adh} and standard deviation for the tiny system are significantly higher than the small, medium, and large grain size tip pairs at 242 ± 154 mJ/m^2. The origin of this increase was determined through the visualization and analysis of the atomic trajectories. Figures 7 and 8 present atomic snapshots and plots of the number of bonds broken and normal force versus time for the tiny (1.1 nm grain size) system for an example IHR cycle with a low (Figure 7) W_{adh} of 56.7 mJ/m^2 and with a high (Figure 8) W_{adh} of 407.3 mJ/m^2. In Figures 7a and 8a, the first snapshot was taken at the simulation time that corresponds with the force just reaching $F_{pull\text{-}off}$ during retraction. The second snapshot was taken shortly after the complete separation of the two tips. In the simulation with the low W_{adh}, the snapshots in Figure 7a show that the two tips cleanly separate after contact. To aid visualization, Mo and S atoms in the opposing tips are colored blue and green and red and yellow, respectively. For the high W_{adh}, the snapshots show significant delamination and grand boundary rupture of the MoS_2 layers as well as apparent bonding between the opposing tips during retraction, as seen in Figure 8a. The process shown in Figure 8a closely resembles the TEM images presented in Figure 4b. After separation, most of the delaminated MoS_2 readheres to the surface of each tip. Some MoS_2 has also transferred between the opposing tips. One small MoS_2 fragment is seen floating free in the vacuum space between the two tips.

Tip−tip covalent bond formation was quantified using a distance-based cutoff that assumes bonding has occurred when pairs of atoms belonging to the opposing tips were within 0.365 0.265, or 0.29 nm for Mo−Mo, S−S, or Mo−S pairs, respectively. These values represent points halfway between

https://doi.org/10.1021/acsami.4c03208
ACS Appl. Mater. Interfaces 2024, 16, 30506−30520

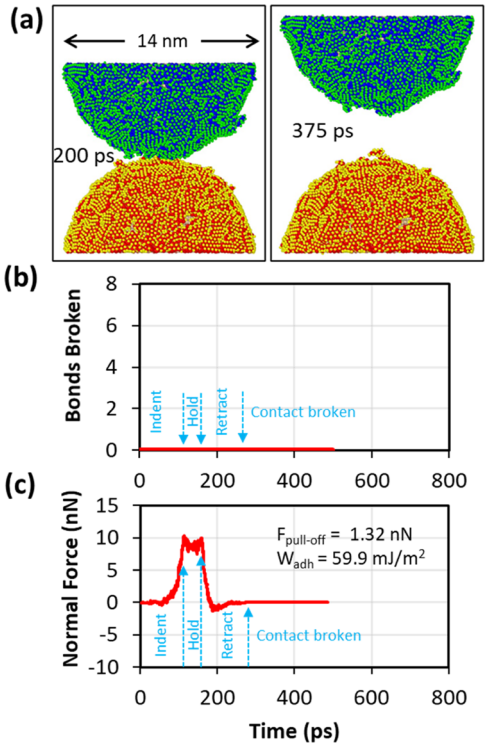

Figure 7. Analysis of the contact behavior of tiny grain size probe tips, where the W_{adh} was low (56.7 mJ/m^2). (a) Snapshots of the atomic trajectories taken at times corresponding to $F_{pull\text{-}off}$ and after complete separation. To aid in visualization, Mo and S atoms belonging to the lower tip are colored red and yellow, respectively, while Mo and S atoms belonging to the upper tip are colored blue and green, respectively. A movie showing entire cycle is shown Video 3 in the Supporting Information. (b) Number of bonds broken and (c) normal force as a function of time for a simulation configuration that resulted in low W_{adh}. In panels (b) and (c), the approach starts at 0 ps; the maximum normal force is reached at 113 ps, and retraction begins at 163 ps. The start and stop of each stage of the IHR cycle are indicated by the blue arrows. All MD visualizations were made using Ovito.[49]

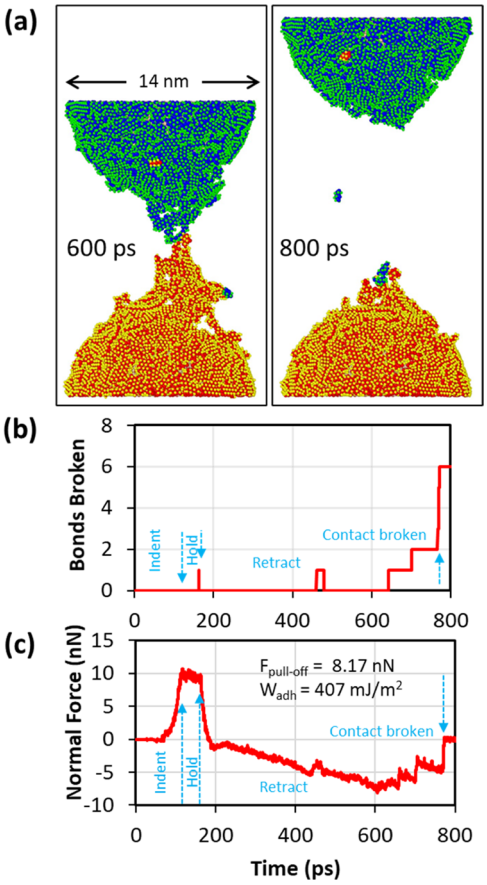

Figure 8. Analysis of the contact behavior of tiny grain size probe tips, where the W_{adh} was high (407.3 mJ/m^2). (a) Snapshots of the atomic trajectories take at times corresponding to $F_{pull\text{-}off}$ and after complete separation. To aid in visualization, Mo and S atoms belonging to the lower tip are colored red and yellow, respectively, while Mo and S atoms belonging to the upper tip are colored blue and green, respectively. A movie showing entire cycle is shown Video 7 in the Supporting Information. (b) Number of bonds broken and (c) normal force as a function of time for a simulation configuration that resulted in high W_{adh}. In panels (b) and (c), the approach starts at 0 ps; the maximum normal force is reached at 121 ps; and retraction begins at 171 ps. The start and stop of each stage of the IHR cycle are indicated by the blue arrows.

the inner and outer cutoff radii for the covalently bonded interaction terms in the Stewart and Spearot[45] reactive empirical bond-order potential for MoS_2. We have applied similar distance-based bond analysis methods for other covalent systems modeled with bond-order potentials.[46−48] The number of bonds broken during separation is shown in Figures 7b and 8b.

When W_{adh} is low, no tip−tip bonds broke as observed in Figure 7b, because no such bonds formed in the first place and no bonds existed at the end of the IHR cycle. Correspondingly, the force−separation curve is relatively short-ranged in Figure 7c, with the tip separating completely at 270 ps at a separation distance of 0.5 nm. The W_{adh} calculated for the simulation shown in Figure 7 is 59.9 mJ/m^2.

When W_{adh} is high, Figure 8b shows that up to six bonds break during separation. Each bond breaking event corresponds closely to sudden drops in the magnitude of the attractive normal force, as seen in Figure 7c. By inspection, the formation of covalent bonds between the edges of MoS_2 grains between the two tips is clearly responsible for the increase in the pull-off force and hence the W_{adh}. However, the extended range of the interaction during retraction is due to delamination and reorientation of the MoS_2 coating along the loading axis during separation. Final separation occurs just after 770 ps, which corresponds to a separation distance of 10.8 nm. The W_{adh} was calculated to be 407 mJ/m^2. Tip-to tip covalent bonding was not observed in any of the small, medium, or large grain size simulations.

We have previously shown that $F_{pull\text{-}off}$ is a linear combination of the following effects

$$F_{pull-off} = F_{BOND} + F_{vdW,nonflat} - F_{dev}$$

where F_{BOND} is the force due to covalent bonding between tips, $F_{vdw,nonflat}$ is the van der Waals force for the continuum geometry without defects, and F_{dev} is the deviation force due to all nonideal effects (defects, step edges, roughness, etc[48]). We found that when bonding is present, even in small amounts, F_{BOND} dominates the pull-off force and W_{adh}. The same is true in the present work. In the simulations shown in Figures 7 and 8, no bonding was observed in the system shown in Figure 7. $F_{pull\text{-}off}$ and W_{adh} are 1.32 nN and 59 mJ/m^2, respectively. The same system under different starting conditions is shown in Figure 8. In this case, six bonds formed. $F_{pull\text{-}off}$ and W_{adh} are 8.17 nN and

https://doi.org/10.1021/acsami.4c03208
ACS Appl. Mater. Interfaces 2024, 16, 30506−30520

369 mJ/m^2, respectively. Assuming F_{dev} for each system is approximately the same, the contribution due to bonding can be approximated as

$$F_{BOND} = F_{pull\text{-}off} - (F_{vdW,nonflat} - F_{dev})$$
$$= 6.85 \text{ nN (or } 310 \text{ mJ/m}^2\text{)}$$

In other words, bonding makes up 84% of the total force. This works out to an average contribution of 1.14 nN per bond broken. The force required to break a covalent bond is much greater than the force required to separate two surfaces upon which van der Waals forces alone act. As expected, F_{BOND} dominates the $F_{pull\text{-}off}$ even when only a few bonds are present.

The medium grain size tip pair shows an interesting behavior, which is perhaps unique to 2D materials. As mentioned above, the force−separation curve for the medium grain size [green line in Figure 6] shows hysteresis during unloading. As indicated by the error bars in Figure 6d, the W_{adh} for the medium grain size has a larger standard deviation (±23 mJ/m^2) relative to those for the small (±8 mJ/m^2) and large (±5 mJ/m^2) grain sizes, even though the average W_{adh} values for the three are similar. Closer inspection of the individual force−separation curves for each of the six medium grain size runs shows the curves fall into two categories: one set with low adhesion and a second set with high adhesion. Representative curves (run 1 and run 4) from each set are presented in Figure 9a. Movies for the MD simulations corresponding to runs 1 and 4 are provided in Videos 5 and 8 in the Supporting Information. Only the unloading portion of the curves is shown. Run 4 has a lower pull-off force and shorter interaction range, with complete separation occurring at 0.6 nm. Run 1 has a larger pull-off force and a much longer interaction range with complete separation occurring at 2.25 nm. In light of the results presented for the tiny grain size systems, one might assume that higher pull-off and longer interaction range are related to bonding between the tips; however, the bonding analysis shows that no covalent bonds form between the two tips in any of the six medium grain size simulations. Instead, the origin was found to be frictional in nature. Figure 9b shows an atomic snapshot of the medium grain size tip pair during the separation stage of run 1. The atomic coordinates of the tip pair have been rotated by 98° clockwise about the z-axis to facilitate clearer viewing. As the pair of tips separates, a flake of MoS_2 partially delaminates from each opposing surface, facilitated by fracture along grain boundaries. These flakes adhere to one another. As the separation between tips grows, the two opposing flakes slide across one another before eventually separating. After separation, the flakes readhere and return to their original location (see Video 5 in the Supporting Information). Because the two flakes are oriented at an angle relative to the load axis, both the interlayer van der Waals attractive forces acting normally to the pair of flakes and frictional forces due to sliding acting along the plane of contact contribute to the normal force between the tip pairs. The off-axis orientation also gives rise to shear forces. The lateral force in the rotated coordinate system ($F_{x'} = F_x \cos(\theta) + F_y \sin(\theta)$), where $\theta = 98°$ during the separation stage, is shown in Figure 9c. The trace of this force shows periodic peaks and valleys typical of friction between materials in commensurate contact.[50,51] The peak-to-peak distance is approximately 0.2 nm, a near match to the underlying lattice structure. Oviedo et al. in their study of shear-stress-induced interlayer sliding in MoS_2 report similar lattice corrugation effects during parallel sliding of stacks of MoS_2.[52] Tang et al. observed both sliding and kinking of layers during delamination

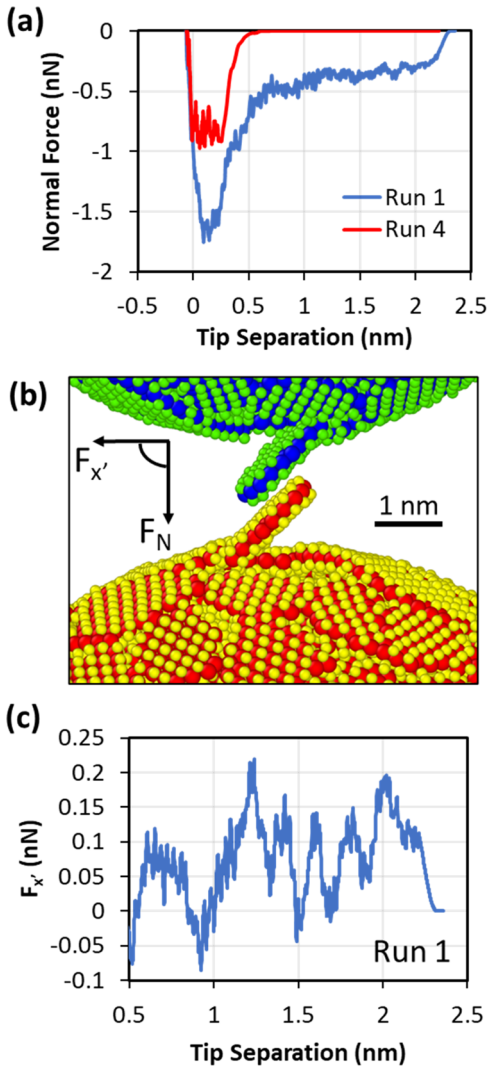

Figure 9. (a) Force−displacement curves for the two cases during tip retraction for the medium grain size probe tips, where the W_{adh} was high (run 1, 93.3 mJ/m^2) and low (run 4, 43.9 mJ/m^2). Movies for the MD simulations corresponding to runs 1 and 4 are provided in Videos 5 and 8 in the Supporting Information. (b) An atomic snapshot taken during the separation stage of run 1, showing opposing MoS_2 layer delamination sliding past one another. To better illustrate the layer alignment, the tip pair was rotated by $\theta = 98°$ clockwise about the z-axis. (c) Trace of the lateral force $F_{x'} = F_x \cos(\theta) + F_y \sin(\theta)$ in the rotated coordinate system during separation in run 1, showing evidence of stick−slip motion.

and suggested that when the length of the crystal is smaller, as is the case for our simulations, the layers are more likely to slide as opposed to kink.[28] Tang et al.'s observations were based on a separation mode driven by a peeling mechanism, whereas separation in our simulations is driven by pure tension.

Effect of Repeated Contact on Adhesion. To study the effect of repeated indentations, the first of the six random starting configurations for each set of tip pairs was repeatedly brought in and out of contact at the same location a total of six times. After each run, any atoms that transferred across the interface between the tip pairs were reassigned to the receiving tip, and the IHR procedure was restarted. The W_{adh} is plotted for each tip pair plotted in Figure 10a. Again, small, medium, and large grain size tip pairs showed consistently low W_{adh} and no covalent bond formation over repeated contacts. We estimate

https://doi.org/10.1021/acsami.4c03208
ACS Appl. Mater. Interfaces 2024, 16, 30506−30520

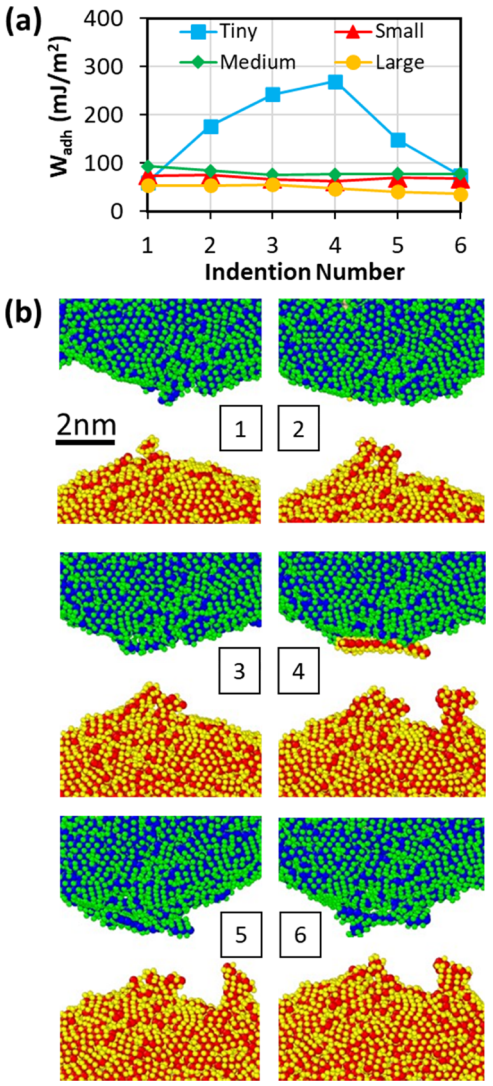

Figure 10. (a) W_{adh} for each repeated indentation and (b) cropped views of the tiny grain size tip pair system showing the apex of the tip pairs after complete separation for each repeated indentation. A significant transfer of atoms happens after the fourth repeated contact. To save space in the graphic, the gap between the upper and lower tips was artificially reduced. The actual gaps after final separation were typically much larger, as seen in Figures 7 and 8

the mean interfacial compressive stress at the maximum load using the continuum DMT model to be 4.7 GPa (see the Supporting Information for details). Thus, for these grain sizes, the coatings showed a high degree of stability, despite the high amount of mechanical stress applied.

In the case of the tiny grain size, the W_{adh} increased steadily until dropping after the fourth indentation. To investigate the origin of this drop, atomistic snapshots were taken after each IHR cycle and are shown in Figure 9b. The images have been cropped to show only the apex of each tip. Visualization shows the transfer of a relatively large MoS_2 monolayer flake consisting of 43 Mo and 81 S atoms (approximately 3 nm by 1 nm in size) after the fourth contact (Figure 10b, panel 4). As before, covalent bonding between the edges of MoS_2 grains on opposing tips appears to be responsible for the increase in the adhesion and transfer of atoms and flakes across the interface. By coincidence, the adhesion between the tiny grain size in the first randomized starting configuration was low. In light of the large standard deviation in the W_{adh}, we observed in the randomized starting conditions for the tiny grain size system (see Figure 6d), and we ran several sets of repeated indentations from the randomized starting conditions. The same trend was observed in each case: the W_{adh} increased with increasing indention cycles, and a drop in adhesion occurred after a large transfer event. The cause of the increase in W_{adh} with increasing cycles is still unclear although it appears to be due to rearrangements in the MoS_2 structure due to the contact pressure. The drop in adhesion at the fifth and sixth cycle is clearly correlated with the transfer of the large flat MoS_2 flake seen on the surface after run 4 (see Figure 10b, frame 4). The flattened nature of the transferred material likely lowers the probability of bonding as a smaller overall edge is exposed. It is also possible that the protruding flake lowers the apparent contact area and consequentially reduces the pull-off force, which results in a lower W_{adh}.

CONCLUSIONS

We have shown that adhesive behavior between self-mated nanoscale silicon asperities coated with ultrathin MoS_2 films depends on the grain size and orientation of the MoS_2 films and that this dependence arises from the probability of interfacial bond formation. In applications where MoS_2 serves as the substrate material (*e.g.*, flexible electronic devices and sensors), where consistent and reproduceable adhesion is desirable, the results shown here indicate that adhesion can be reduced by creating larger MoS_2 grains. Experimentally, this can be achieved by postdeposition thermal annealing as has been previously shown by Glavin et al.[17]

The experimental results for repeated tip-to-tip contact show variable adhesion in the case of nominally amorphous coatings deposited at 22 °C and steadily increasing adhesion in the case of nanocrystalline coatings deposited at 400 °C. The average W_{adh} measured experimentally between tip pairs is significantly larger (932 ± 647 and 604 ± 323 mJ/m^2 for nominally amorphous tip pair 1 and nanocrystalline tip pair 2, respectively) than previously reported literature values for W_{adh}.[26,27,53] Closely matched MD simulations show that the anomalously large W_{adh} arises from covalent bonding between sites at grain boundaries in polycrystalline MoS_2 coatings. Bonding is not observed between the tip pairs with small (1.5 nm), medium (2.0 nm), and large (4.4 nm) grain sizes; however, in the experiments, material transfer clearly was present between the nanocrystalline MoS_2 coatings, where the MoS_2 grain size was approximately 6 nm. Here, the simulation and experiment appear to disagree. This discrepancy can be explained the following way. Previous work has shown that covalent bonding is stochastic and has two general factors, opportunity and thermal fluctuation, that combine to produce a bonding probability.[47,54] First, the time in contact is much longer in the experiments (typically 40 s) than in the simulations (50 ps), which will lead to a far larger probability of bond formation during contact due to thermal fluctuations. Second, an opportunity presents itself here, where there are defects present in the form of sites at grain boundaries on both tips that are near each other. Figure 11 shows a schematic representation of the contact patch for the tiny and large MoS_2 grain size coating tips. Here, the contact patch diameter is approximately 2 nm. The dashed black lines represent the grain boundaries for the lower tip, while the red lines represent the grain boundaries for the upper tip, in this case a mirrored image. Potential bonding sites are represented schematically in Figure 11 as points where the red and black lines cross. For the tiny grain size system, the red and black lines

https://doi.org/10.1021/acsami.4c03208
ACS Appl. Mater. Interfaces 2024, 16, 30506−30520

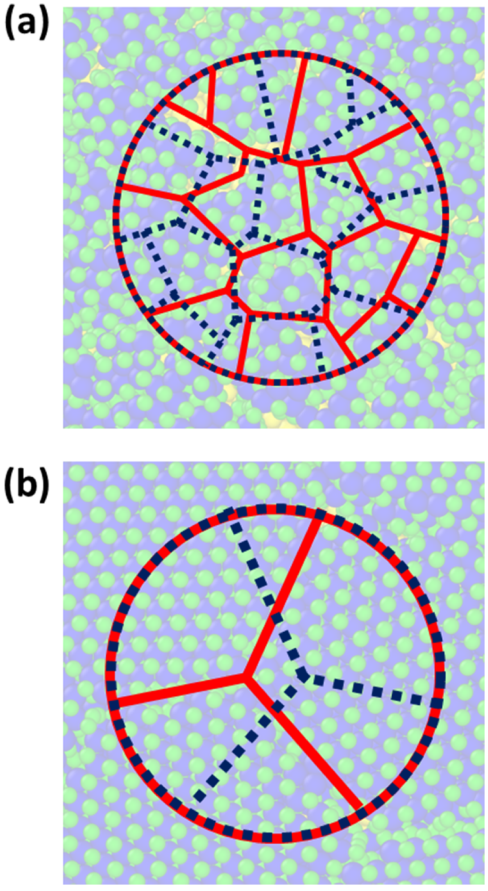

Figure 11. Schematic representation of the MoS_2 grain boundaries in the contact patch for the lower tip (red solid line) and upper tip (black dashed lines) superimposed over the atomic structure of the lower tip for (a) the tiny grain size tip and (b) the large grain size tip. For scale, the diameter of the contact patch is approximately 2.0 nm. Each crossing point of the red and black lines is a potential location for intertip bond formation.

intersect in many places relative to the large grain size system, which indicates that the opportunity for bonding and hence probability for bonding, all other things equal, is much higher for the tiny grain size system. In the experimental contact measurements, the tips have a radius 2−7 times that of the simulations [see Figure 2], and thus, when the two tips are in contact, the contact patch and number of intersecting grains will be larger and hence the probability for bonding will be higher. In the case of the nominally amorphous tips, the large variability in adhesion is likely due to the alignment of the MoS_2 edges. The TEM images [see Figure 2 (a,b)] show that some of the MoS_2 is aligned such that the edges point outwardly normal to the tip surface. This should lead to an enhanced probability for bonding at these exposed edges. In addition, strain in the films due to curvature is accommodated at the grain boundaries in the form of kinks. Reactivity at the boundaries may also be enhanced due to the strained nature of the bonding between grains at these kinks.

Another factor which may cause increased adhesion in the experiments is the exposure of a clean surface after transfer or removal of the material from the surface. There are at least two possible scenarios. First, any flattening or blunting of tip by the removal, disruption, or transfer of the material could increase the true area of contact and should increase adhesion. Conversely, roughening of the tip should decrease adhesion due to the reduction in the true contact area. Second, the exposure of fresh unterminated surfaces due to material transfer may also lead to an increase in the W_{adh} due to the possibility of the exposure of new unterminated edges. Previous studies of contact between other covalent materials, such as diamond, diamond-like carbon,[46,47] and silicon,[48,57] suggest that the degree of surface termination plays a major role in adhesion. However, in MoS_2, the basal plane tends to be inert with only the edges available for bonding. Hence, the second scenario is likely to have a minimal effect, as area around the edge of the grain is low relative to the area of the basal plane. The simulations seem to support the first option. The simulations suggest, as shown in Figure 10, in panel 4, the transfer of a MoS_2 flake may cause a reduction in the W_{adh} because of reduction in the true contact area due to roughening of the tip surface. In contrast, flattening should have the opposite effect. Flattening of the overall contact was not observed. Additional simulations will be needed to further investigate these behaviors.

Finally, W_{adh} values reported previously in the literature are for large single crystal flakes of mechanically exfoliated MoS_2. Here, we have presented findings for W_{adh} for nominally amorphous and nanocrystalline MoS_2 as commonly observed in thin, vapor-deposited films. Also, our experiments and

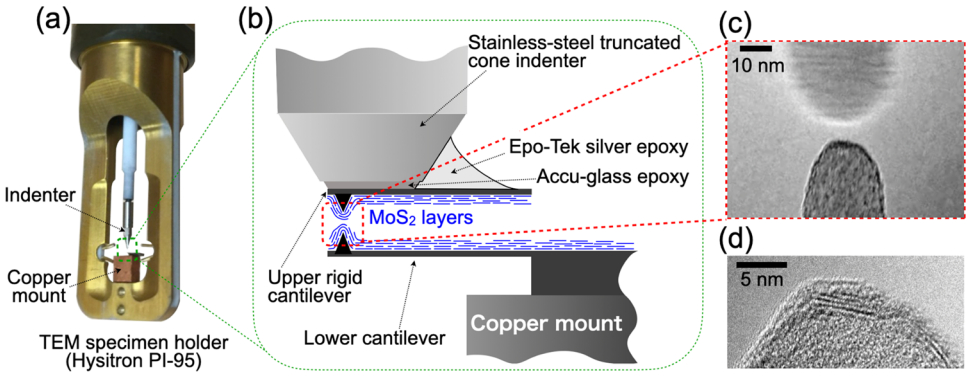

Figure 12. Experimental setup. (a) The magnified front end of the picoindenter (Hysitron PI-95) showing the AFM chip with a flexible cantilever (located on top of the copper mount) facing the indenter, which has an AFM cantilever rigidly attached (the cantilever is too small to see in this image). (b) Schematic of the AFM chip and cantilever across the cantilever on the indenter. The lower cantilever is free to deflect due to forces experienced by the tip, while the upper cantilever cannot deflect due to the epoxy. (c) TEM image of the two AFM probe tips. (d) TEM image of the apex of the lower probe tip in panel (c), showing that it is terminated with MoS_2 layers.

https://doi.org/10.1021/acsami.4c03208
ACS Appl. Mater. Interfaces 2024, 16, 30506−30520

simulations are for primarily compressive and tensile loading, i.e., normal to the MoS_2 basal plane, while some prior literature involves peeling or shearing, *i.e.*, with some forces and/or displacements applied parallel to the basal plane. Adhesive behavior for all loading directions is of interest; an advantage of focusing purely on normal loads and displacements is that it simplifies the mechanics required to interpret the results and provides a well-defined loading geometry to consider as a baseline.

METHODS

Sample Preparation. Prior to MoS_2 application, a series of single-crystal silicon cantilevers (contact mode AFM probes HQ:CSC37/No Al, MikroMasch USA) were prepared and characterized by TEM to confirm that the tips were clean and sharp (with a single protrusion, < 20 nm in radius). AFM cantilevers were maintained at 22 °C during physical vapor deposition of ultrathin amorphous MoS_2. For synthesis of nanocrystalline MoS_2, tips were heated to 400 °C in an ultrahigh purity argon ambient and maintained at that temperature during growth using processes described in refs 55,56. Briefly, a pulsed power supply (65 kHz) and magnetically attenuated energetic particle flux were used to sputter ultrathin continuous films from a MoS_2 target on cantilever tips with high radii of curvature. HRTEM imaging was then used to evaluate the crystalline structure of the MoS_2 layers and their interface with the underlying silicon probe tips.

Adhesion Measurements. To study the contact and adhesion behavior of MoS_2 at the nanoscale, we made use of a customized *in situ* TEM/AFM nanoindenter. The setup for this method is illustrated in Figure 12. A PI-95 ECR Bruker-Hysitron (Eden Prairie, MN) Picoindenter [Figure 12a] was used inside a JEOL (Akishima, Tokyo, Japan) F200 TEM to make and break contact between two opposing MoS_2-coated AFM tips using the protocol previously described by Milne[57] [Figure 12b]. With this method, contact and separation can be conducted with live TEM imaging (Figure 12c). In addition, HRTEM can be conducted on the tips before and after each contact (Figure 12d). This allows observation of the phenomena occurring during contact, including elastic and plastic deformation, damage, and material transfer. The attractive and repulsive forces during contact are also determined by using the TEM image to measure the deflection of the lower cantilever, which is converted to a normal force by using the normal spring constant k_n (0.3 N/m) measured using the Sader method.[58] When combined with measurements of the contact geometry, these measurements can be used to determine the work of adhesion.[38] For imaging, a relatively low accelerating voltage of 80 kV was used to avoid electron beam induced damage to the films.

MD Structure Generation. The methods used to generate the initial structures for the MD simulation and methods to simulate adhesion are given below. While it may be possible to model the deposition and growth process of the nanocrystalline and amorphous MoS_2 films using modern reactive empirical potentials, to do so would be very time-consuming and lacks the control required to approximate experimental conditions. In our approach, we have developed a Voronoi polyhedron method to create nanocrystalline starting configurations that give control over the number of layers, grain structure, and grain size of the crystalline MoS_2 domains. The goal of this approach is to match the known experimental aspects of the tip geometry and film structures as closely as possible. Since an amorphous structure with small crystalline regions was observed in the TEM analysis of the MoS_2 film deposited at 22 °C, our aim was to create starting the MD structure with grains so small that the amorphous character dominates; this will be used to represent the amorphous film in our simulations.

In our Voronoi polyhedron method, a set of randomized spherical coordinates are generated on the surface of a hemispherical shell. Each point represents the center of a MoS_2 crystallite. Next, sheets of single layer hexagonal MoS_2 were tessellated over the hemisphere by centering the MoS_2 sheets at each random cell point. Prior to placement, sheets are rotated randomly in-plane to create a randomized grain orientation. Next, each grain is warped geometrically such that its curvature matches the desired hemispherical radius. At this stage, atoms from overlapping grains were removed by eliminating any atoms that extend beyond the grain boundaries of a given cell point. The grain boundaries of each crystal are taken as the edges of the polygon that makes up the Voronoi cell. These cell edges are defined as the line normal to the vector connecting adjacent grain centers, located at a distance centered at the halfway point between neighboring grain centers. An additional constraint is applied, such that pairs of Mo−Mo or Mo−S atoms along adjacent grain edges can be no closer than 0.3 or 0.24 nm, respectively. This cutoff eliminates atom overlaps and associated numerical instabilities in the MD simulations. To create multilayer films, this process is repeated for successively larger radii shells. To accommodate van der Waals (vdW) interactions, the radius of the first MoS_2 shell is set such that the distance between the innermost S layer is 0.35 nm from the outermost Si atoms on the hemispherical base tip. Sequential MoS_2 layers are added radially in increments of the MoS_2 interlayer spacing (0.68 nm each).

Grain Size Control. Experimentally, the MoS_2 domain size and structure (varying amounts of crystalline and amorphous character) can be controlled through the annealing conditions.[33−35] In the method for MD structure generation described above, we can exert effectively equivalent control by varying the spacing between the randomly selected grain centers and the number of grain centers present in a given surface area. The average grain area is estimated by dividing the hemispherical area by the number of grain centers. If grains are assumed to be roughly circular, the grain diameter, d, can be approximated as

$$d = 2R\sqrt{\frac{2}{n}} \tag{3}$$

where R is the hemisphere (tip) radius and n is the number of grain centers on the hemisphere. To control grain size and distribution, an exclusionary cutoff distance was imposed during the random selection of grain centers. In this method, the position of each new randomly selected grain center is compared to all previous centers. If the distance between the new point and any previously selected point is beyond the cutoff distance, the point is saved, and the process continues. If the distance between the new point and any other point is less than the cutoff, the point is discarded and a new random point is selected. This process continues until either the desired number of grain centers is reached or an excessive number of tries (>100) is reached. The number of grains and the cutoff length can be used in conjunction to fine-tune the average grain size and the distribution of grain sizes.

After the initial configurations are generated, the energy of each system is minimized using the Polak−Ribiere conjugate gradient approach.[59] The system is then equilibrated at 300 K for 50 ps. Temperature was maintained via a Berendsen thermostat.[60] The Sandia Large-scale Atomic/Molecular Massively Parallel Simulator (LAMMPS)[61] is used to run the simulations. To describe the interatomic interactions, a hybrid pair-style model is employed. The Tersoff-94[62] potential is used to model the Si interactions in the base tip. The interactions between Mo and S atoms are handled using a REBO-style potential for MoS_2 created by Liang[63] and subsequently updated by Stewart and Spearot.[45] This potential recreates covalent bonding and dynamic bond formation and breaking events likely to occur at grain edges by employing a modified version of the second-generation Brenner[64] reactive empirical bond-order potential fit for MoS_2. This potential includes a switchable 12−6 Lennard-Jones (LJ) potential[65,66] to capture the long-range, nonbonded van der Waals interactions between adjacent MoS_2 layers. The smooth transition between bonded and nonbonded interactions between atoms was achieved by using a cubic spline switching function, allowing reactions between layers to occur under the right conditions. This potential produces a reasonable value for the W_{adh} of single-crystal bulk 2H-MoS_2 (248 mJ/m^2). Details regarding the calculation of bulk MoS_2 are provided in the Supporting Information. The interactions between the Si base tip and MoS_2 are modeled as nonbonded interactions with a 12−6 LJ pair potential. Chemical reactions between the Si base tip and MoS_2 are neglected under the assumption that interactions between

https://doi.org/10.1021/acsami.4c03208
ACS Appl. Mater. Interfaces 2024, 16, 30506−30520

pairs of interacting probe tips will occur between contacting MoS_2 layers and not the base Si probe tips. The LJ parameters were obtained by combining the Mo and S parameters from Jiang et al.[67] with the Si parameters from Rappé et al.[68] using standard mixing rules. The resulting ε and σ parameters for Mo−Si and S−Si pairs are 0.02027 eV and 3.488 Å, respectively. A relatively short LJ cutoff of 2.5σ was applied to limit the range of Si−MoS_2 interactions to the first MoS_2 layer.

Our TEM observations show well-ordered layered conformal coatings of MoS_2 for tip radii above 5 nm. Coatings on tips with radii below 5 nm exhibit significant disorder or nonconformal MoS_2 layers (not shown). Our attempts to simulate tips smaller than 5 nm resulted in delamination of the MoS_2 film during the initial equilibration steps. We hypothesized that the stress required to bend MoS_2 layers to radii smaller than 5 nm exceeds the forces due to van der Waals attraction between MoS_2 and the curved Si surface, which results in partial delamination of the film and disordered growth. Based on this experimental observation and preliminary simulations, a Si tip radius of 5 nm with three layers of MoS_2 is used. These dimensions represent a reasonable compromise between matching the experimental conditions and the computational efficiency. Tips coated with MoS_2 with four different grain sizes were constructed referred to as Tiny, Small, Medium, and Large, having average MoS_2 grain sizes of 1.1 1.5, 2.0, and 4.4 nm, respectively. The resulting tips are shown in Figure 13a. The

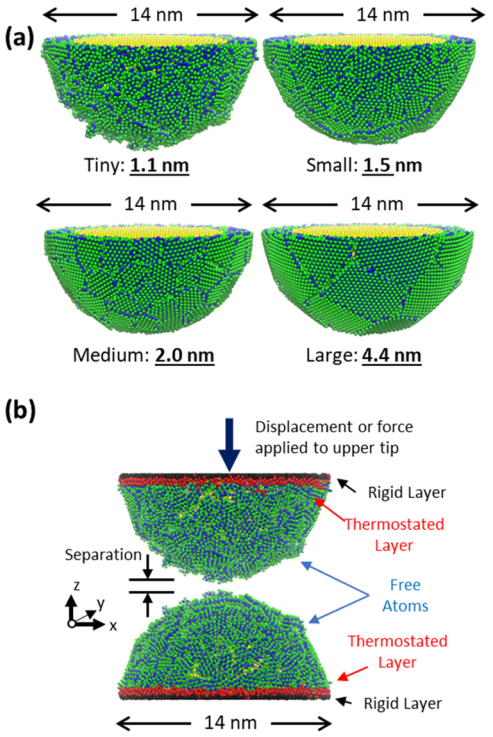

Figure 13. (a) MoS_2 coated Si probe tips with varying grain sizes. Mo, S, and Si atoms are colored blue, green, and yellow, respectively. The probe radius for each tip is ~7 nm. (b) The setup for tip-to-tip contact simulations. The tip pair shown has an MoS_2 grain size of 1.1 nm. Atoms colored black are treated as a rigid body, atoms colored red are temperature-controlled; Mo, S, and Si are colored blue, green, and yellow, respectively. (Note: The *y*-axis points in the direction normal to the page.)

outer radius of the tip after the MoS_2 layers are applied is 7.04 nm, which is approximately the same as the tips shown in Figure 2a,b but about half that of Figure 2c and one-seventh of the tip shown in Figure 2d.

Phonon Density of States Calculation. The method used to calculate the PDOS for the MoS_2 films was previously described by Rouhani et al.[41] and was based on the earlier work of Loong et al.[69] and Varshney et al.[70] First, the system was equilibrated at a constant temperature for 150 ps. Potential energy and temperature converge to steady-state values after approximately 20 ps. Next, the normalized velocity autocorrelation function (VACF) for Mo and S was calculated. The normalized velocity−velocity autocorrelation function for the βth species (β = Mo or S) is given by $\Gamma_\beta(t) = \frac{\langle \sum_{i\beta}^{N\beta} v_{i\beta}(t)\cdot v_{i\beta}(0)\rangle}{\langle \sum_{i\beta}^{N\beta} v_{i\beta}(0)\cdot v_{i\beta}(0)\rangle}$, where $v_{i\beta}$ is the velocity of particle i of species β, N_β is the number of each partical type, and < > is the average over the course of the simulation. The next step is to calculate the Fourier transform of the normalized VACF. The real part of the frequency spectrum from the Fourier transform $F_\beta(\omega) = \int_0^\tau \Gamma_\beta(t)\cos(\omega t)dt$ yields the partial PDOS for each element. Finally, the total PDOS is then taken as the sum of the partial PDOS weighed by the concentration of Mo and S. The contributions from Si in the underlying tip were not included in the total PDOS. The VACF was sampled and output every 0.02 ps. To produce a PDOS spectrum in the frequency range of interest with a resolution comparable to experimentally obtained Raman spectra, a total of 2048 samples were obtained over the course of 40.96 ps of simulation time. The MD simulation was run with a time step size of 0.0005 ps. To reduce noise, the VACF was averaged over ten sampling windows for a total simulation time of 409.6 ps. This results in PDOS spectra with a resolution of 0.814 cm^{-1} and a maximum frequency of 833.33 cm^{-1}. The PDOS for bulk MoS_2 was obtained similarly.

MD Simulations of Adhesion. The general setup for tip-to-tip contact simulations is illustrated in Figure 13b. To start, the tips described above are replicated, flipped over, and placed above one another with an initial separation of 1 nm to create tip pairs with matching grain sizes. This initial separation distance was selected so that the atoms in the two tips are outside the range of the atomic potential initially. Working inward, a 0.2 nm layer of atoms at the top and bottom is held rigid (black atoms). A thermostat is applied to top atoms between 0.2 and 0.7 nm from the top and bottom (red atoms). All other atoms are free to move according to Newton's classical equations of motion. The potentials used to determine the pair−pair interactions are described in the previous section.

The indent-hold-retract (IHR) contact cycle is described as follows: first, the initial configuration is equilibrated at 300 K for 25 ps. The initial temperature is set to 300 K by assigning a randomly generated Gaussian distribution of velocities to each atom in the ensemble (with the exception of the rigid layer atoms). To speed up the initial equilibration stage, a Berendsen thermostat[60] set to 300 K is applied to all unconstrained atoms. Next, the upper tip is brought into contact with the lower tip with a constant velocity of 0.02 nm/ps (20 m/s) until the load reaches 10 nN. During the indentation stage and subsequent steps, the Berendsen thermostat is applied only to atoms located in the regions shown in red in Figure 13b. The thermostat is applied only in the horizontal degrees of freedom (x and y) in the region far from the contact zone to minimize the thermostat's influence on forces in the normal contacting (z) direction. After contact is made, the tips are held in contact at a constant load of 10 nN for 50 ps. The hold step allows for the load to stabilize to a steady state value after initial contact is made. As mentioned above in experiments, the load is held to 0 nN through adhesive forces. This condition is difficult to achieve in the MD simulations due to algorithmic limitations. We selected the relatively low load of 10 nN as it was the lowest practical load, where the contact could be reliably held in contact. Finally, the upper tip is retracted at 0.02 nm/ps until all contact is broken. During the IHR cycle, the force on the upper tip and the tip−tip separation are monitored. The normal force, calculated as the sum of the forces on all atoms present in the upper tip, is collected every 2.5 fs, averaged, and output in 50 fs intervals. To reduce scatter due to random thermal fluctuations, force data is smoothed using a forty-point running average. The separation between the tips is also calculated during the course of the IHR cycle as follows

$$\text{separation} = z_{\text{sep}} - (z_{\text{initial}} - z_{\text{current}}) \quad (4)$$

where z_{sep} is the initial tip separation (set to 1.0 nm), z_{initial} is the initial position of the fixed layer in the upper tip, and z_{current} is the current position of the fixed layer in the upper tip.

https://doi.org/10.1021/acsami.4c03208
ACS Appl. Mater. Interfaces 2024, 16, 30506−30520

■ ASSOCIATED CONTENT

Data Availability Statement

The data that support the findings of this study are available upon reasonable request from the corresponding author.

Supporting Information

The Supporting Information is available free of charge at https://pubs.acs.org/doi/10.1021/acsami.4c03208.

HRTEM video of the first contact between the as-deposited MoS_2 coated AFM probe tips (tip pair 1) (Video 1) (MOV)

HRTEM video of the first contact between the thermally annealed MoS_2 coated AFM probe tips (tip pair 2) (Video 2) (MOV)

MD movie showing the compete indent-hold-retract cycle for the tip probe pair coated with 1.1 nm average grain size (Tiny Run 1) (Video 3) (MOV)

MD movie showing the compete indent-hold-retract cycle for the tip probe pair coated with 1.5 nm average grain size (Small) (Video 4) (MOV)

MD movie showing the compete indent-hold-retract cycle for the tip probe pair coated with 2.0 nm average grain size (Medium Run 1) showing flake delamination during separation. To aid with visualization of the flake delamination the system was rotated by 98° clockwise about the vertical axis (Video 5) (MOV)

MD movie showing the compete indent-hold-retract cycle for the tip probe pair coated with 2.0 nm average grain size (Large) (Video 6) (MOV)

MD movie showing the compete indent-hold-retract cycle for the tip probe pair coated with 1.1 nm average grain size (Tiny Run 4) showing significant tip-to-tip bonding and material transfer (Video 7) (MOV)

MD movie showing the compete indent-hold-retract cycle for the tip probe pair coated with 2.0 nm average grain size (Medium Run 4) showing no flake delamination during separation (Video 8) (MOV)

Movie showing the MD simulation of the separation of bulk MoS_2 with an in-registry layer alignment (Video 9) (MOV)

Movie showing the MD simulation of the separation of bulk MoS_2 with an out-of-registry layer alignment (Video 10) (MOV)

Measurement of the MoS_2 grain size via high-resolution TEM, additional TEM images of the thermally annealed and as-deposited films on AFM probe tips, discussion regarding the calculation of the Tabor parameter, estimation of the contact radius and contact stress and discussion and results from of the calculation work of adhesion for bulk MoS_2 via MD simulation, simulation of offset tips and friction analysis (PDF)

■ AUTHOR INFORMATION

Corresponding Author

J. David Schall − *Department of Mechanical Engineering, North Carolina A&T State University, Greensboro, North Carolina 27411, United States;* orcid.org/0000-0002-3694-9934; Email: jschall@ncat.edu

Authors

Sathwik Reddy Toom − *Department of Mechanical Engineering, North Carolina A&T State University, Greensboro, North Carolina 27411, United States*

Takaaki Sato − *Department of Mechanical Engineering and Applied Mechanics, University of Pennsylvania, Philadelphia, Pennsylvania 19104, United States*

Zachary Milne − *Gatan, Inc., Pleasanton, California 94588, United States*

Rodrigo A. Bernal − *Department of Mechanical Engineering, University of Texas, Dallas, Richardson, Texas 75080, United States;* orcid.org/0000-0001-7517-7781

Yeau-Ren Jeng − *Department of Biomedical Engineering, National Cheng Kung University in Tainan, Tainan 70101, Taiwan;* orcid.org/0000-0001-6787-1538

Christopher Muratore − *Department of Chemical and Materials Engineering, University of Dayton, Dayton, Ohio 45469, United States;* orcid.org/0000-0002-5555-9261

Nicholas R. Glavin − *Materials and Manufacturing Directorate, US Air Force Research Laboratory, Wright-Patterson AFB, Ohio 45433, United States;* orcid.org/0000-0002-9447-7509

Robert W. Carpick − *Department of Mechanical Engineering and Applied Mechanics, University of Pennsylvania, Philadelphia, Pennsylvania 19104, United States;* orcid.org/0000-0002-3235-3156

Complete contact information is available at: https://pubs.acs.org/10.1021/acsami.4c03208

Author Contributions

The MoS_2-coated AFM tips were prepared by C.M. and N.R. The experimental measurements and TEM analysis were conducted by T.S., R.A.B., and Z.M. contributed to the preliminary TEM studies associated with this work. The MD simulations were conducted by S.R.T. and J.D.S. Funding for this work was obtained by R.W.C., Y.-R.J., and J.D.S. S.R.T., J.D.S., T.S., and R.W.C. were responsible for preparing and editing this publication.

Notes

The authors declare no competing financial interest.

■ ACKNOWLEDGMENTS

J.D.S. and R.W.C. would like to acknowledge support from AFOSR/AOARD through Award No. FA2386-18-1-4083. J.D.S. would also like to acknowledge support from the Department of Energy through Award No. DE-SC0023679 and NSF Partnership of the Research and Education in Materials (PREM) program via Grant Number DMR-2122067. R.W.C. would like to acknowledge support from the National Science Foundation under Award No. CMMI- 2041662. J.D.S. and S.R.T. would like to thank Douglas Spearot for providing the LAMMPS subroutines for the MoS_2 interatomic potential.

■ REFERENCES

(1) Cai, S.; Han, Z.; Wang, F.; Zheng, K.; Cao, Y.; Ma, Y.; Feng, X. Review on Flexible Photonics/Electronics Integrated Devices and Fabrication Strategy. *Sci. China Inf. Sci.* **2018**, *61* (6), No. 060410.

(2) Harris, K. D.; Elias, A. L.; Chung, H.-J. Flexible Electronics under Strain: A Review of Mechanical Characterization and Durability Enhancement Strategies. *J. Mater. Sci.* **2016**, *51* (6), 2771−2806.

(3) Hong, Y. J.; Jeong, H.; Cho, K. W.; Lu, N.; Kim, D.-H. Wearable and Implantable Devices for Cardiovascular Healthcare: From Monitoring to Therapy Based on Flexible and Stretchable Electronics. *Adv. Funct. Mater.* **2019**, *29* (19), No. 1808247.

(4) Sang, M.; Kang, K.; Zhang, Y.; Zhang, H.; Kim, K.; Cho, M.; Shin, J.; Hong, J.-H.; Kim, T.; Lee, S. K.; Yeo, W.-H.; Lee, J. W.; Lee, T.; Xu, B.; Yu, K. J. Ultrahigh Sensitive Au-Doped Silicon Nanomembrane

Based Wearable Sensor Arrays for Continuous Skin Temperature Monitoring with High Precision. *Adv. Mater.* **2022**, *34* (4), No. 2105865.
(5) Gelinck, G. H.; Huitema, H. E. A.; van Veenendaal, E.; Cantatore, E.; Schrijnemakers, L.; van der Putten, J. B. P. H.; Geuns, T. C. T.; Beenhakkers, M.; Giesbers, J. B.; Huisman, B.-H.; Meijer, E. J.; Benito, E. M.; Touwslager, F. J.; Marsman, A. W.; van Rens, B. J. E.; de Leeuw, D. M. Flexible Active-Matrix Displays and Shift Registers Based on Solution-Processed Organic Transistors. *Nat. Mater.* **2004**, *3* (2), 106−110.
(6) Lipomi, D. J.; Tee, B. C.-K.; Vosgueritchian, M.; Bao, Z. Stretchable Organic Solar Cells. *Adv. Mater.* **2011**, *23* (15), 1771−1775.
(7) Lei, Y.; Zhang, T.; Lin, Y.-C.; Granzier-Nakajima, T.; Bepete, G.; Kowalczyk, D. A.; Lin, Z.; Zhou, D.; Schranghamer, T. F.; Dodda, A.; Sebastian, A.; Chen, Y.; Liu, Y.; Pourtois, G.; Kempa, T. J.; Schuler, B.; Edmonds, M. T.; Quek, S. Y.; Wurstbauer, U.; Wu, S. M.; Glavin, N. R.; Das, S.; Dash, S. P.; Redwing, J. M.; Robinson, J. A.; Terrones, M. Graphene and Beyond: Recent Advances in Two-Dimensional Materials Synthesis, Properties, and Devices. *ACS Nanosci. Au* **2022**, *2* (6), 450−485.
(8) Novoselov, K. S.; Mishchenko, A.; Carvalho, A.; Castro Neto, A. H. 2D Materials and van Der Waals Heterostructures. *Science* **2016**, *353* (6298), No. aac9439.
(9) Radisavljevic, B.; Radenovic, A.; Brivio, J.; Giacometti, V.; Kis, A. Single-Layer MoS2 Transistors. *Nat. Nanotechnol.* **2011**, *6* (3), 147−150.
(10) Chan, M. Y.; Komatsu, K.; Li, S.-L.; Xu, Y.; Darmawan, P.; Kuramochi, H.; Nakaharai, S.; Aparecido-Ferreira, A.; Watanabe, K.; Taniguchi, T.; Tsukagoshi, K. Suppression of Thermally Activated Carrier Transport in Atomically Thin MoS2 on Crystalline Hexagonal Boron Nitride Substrates. *Nanoscale* **2013**, *5* (20), 9572−9576.
(11) Savan, A.; Pflüger, E.; Voumard, P.; Schröer, A.; Simmonds, M. Modern Solid Lubrication: Recent Developments and Applications of MoS2. *Lubr. Sci.* **2000**, *12* (2), 185−203.
(12) Saidi, M. Z.; El Moujahid, C.; Pasc, A.; Canilho, N.; Delgado-Sanchez, C.; Celzard, A.; Fierro, V.; Kouitat-Njiwa, R.; Chafik, T. Enhanced Tribological Properties of Wind Turbine Engine Oil Formulated with Flower-Shaped MoS2 Nano-Additives. *Colloids Surf. Physicochem. Eng. Asp.* **2021**, *620*, No. 126509.
(13) Goel, N.; Bera, J.; Kumar, R.; Sahu, S.; Kumar, M. MoS2-PVP Nanocomposites Decorated ZnO Microsheets for Efficient Hydrogen Detection. *IEEE Sens. J.* **2021**, *21* (7), 8878−8885.
(14) Kong, R.-M.; Ding, L.; Wang, Z.; You, J.; Qu, F. A Novel Aptamer-Functionalized MoS2 Nanosheet Fluorescent Biosensor for Sensitive Detection of Prostate Specific Antigen. *Anal. Bioanal. Chem.* **2015**, *407* (2), 369−377.
(15) Butler, S. Z.; Hollen, S. M.; Cao, L.; Cui, Y.; Gupta, J. A.; Gutiérrez, H. R.; Heinz, T. F.; Hong, S. S.; Huang, J.; Ismach, A. F.; Johnston-Halperin, E.; Kuno, M.; Plashnitsa, V. V.; Robinson, R. D.; Ruoff, R. S.; Salahuddin, S.; Shan, J.; Shi, L.; Spencer, M. G.; Terrones, M.; Windl, W.; Goldberger, J. E. Progress, Challenges, and Opportunities in Two-Dimensional Materials Beyond Graphene. *ACS Nano* **2013**, *7* (4), 2898−2926.
(16) Glavin, N. R.; Rao, R.; Varshney, V.; Bianco, E.; Apte, A.; Roy, A.; Ringe, E.; Ajayan, P. M. Emerging Applications of Elemental 2D Materials. *Adv. Mater.* **2020**, *32* (7), No. 1904302.
(17) Glavin, N. R.; Chabak, K. D.; Heller, E. R.; Moore, E. A.; Prusnick, T. A.; Maruyama, B.; Walker, D. E., Jr.; Dorsey, D. L.; Paduano, Q.; Snure, M. Flexible Gallium Nitride for High-Performance, Strainable Radio-Frequency Devices. *Adv. Mater.* **2017**, *29* (47), No. 1701838.
(18) Yue, Q.; Kang, J.; Shao, Z.; Zhang, X.; Chang, S.; Wang, G.; Shiqiao, Q.; Li, J. Mechanical and Electronic Properties of Monolayer MoS2 under Elastic Strain. *Phys. Lett. A* **2012**, *376*, 1166−1170.
(19) Trainer, D. J.; Zhang, Y.; Bobba, F.; Xi, X.; Hla, S.-W.; Iavarone, M. The Effects of Atomic-Scale Strain Relaxation on the Electronic Properties of Monolayer MoS2. *ACS Nano* **2019**, *13* (7), 8284−8291.
(20) Israelachvili, J. N. *Intermolecular and Surface Forces*, 3rd ed.; Academic Press: Burlington, MA, 2011.
(21) Didziulis, S. V.; Fleischauer, P. D.; Soriano, B. L.; Gardos, M. N. Chemical and Tribological Studies of MoS2 Films on SiC Substrates. *Surf. Coat. Technol.* **1990**, *43*−*44*, 652−662.
(22) Hilton, M. R.; Bauer, R.; Fleischauer, P. D. Tribological Performance and Deformation of Sputter-Deposited MoS2 Solid Lubricant Films during Sliding Wear and Indentation Contact. *Thin Solid Films* **1990**, *188* (2), 219−236.
(23) Fleischauer, P. D.; Hilton, M. R.; Bauer, R. Paper V (i) Effects of Microstructure and Adhesion on Performance of Sputter-Deposited MoS2 Solid Lubricant Coatings. In *Tribology Series*; Dowson, D.; Taylor, C. M.; Godet, M., Eds.; Mechanics of Coatings; Elsevier, 1990; *17*, pp 121−128. DOI: 10.1016/S0167-8922(08)70248-7.
(24) Banday, S.; Reshi, B. A.; Wani, M. F. Adhesion Strength and Tribological Property of Self-Lubricating Si/MoS2 Nanocoating by Pulsed Laser Deposition Method. *Ceram. Int.* **2021**, *47* (24), 35260−35267.
(25) Rokni, H.; Lu, W. Direct Measurements of Interfacial Adhesion in 2D Materials and van Der Waals Heterostructures in Ambient Air. *Nat. Commun.* **2020**, *11* (1), 5607.
(26) Lloyd, D.; Liu, X.; Boddeti, N.; Cantley, L.; Long, R.; Dunn, M. L.; Bunch, J. S. Adhesion, Stiffness, and Instability in Atomically Thin MoS2 Bubbles. *Nano Lett.* **2017**, *17* (9), 5329−5334.
(27) Deng, S.; Gao, E.; Xu, Z.; Berry, V. Adhesion Energy of MoS2 Thin Films on Silicon-Based Substrates Determined via the Attributes of a Single MoS2 Wrinkle. *ACS Appl. Mater. Interfaces* **2017**, *9* (8), 7812−7818.
(28) Tang, D.-M.; Kvashnin, D. G.; Najmaei, S.; Bando, Y.; Kimoto, K.; Koskinen, P.; Ajayan, P. M.; Yakobson, B. I.; Sorokin, P. B.; Lou, J.; Golberg, D. Nanomechanical Cleavage of Molybdenum Disulphide Atomic Layers. *Nat. Commun.* **2014**, *5* (1), 3631.
(29) Fang, Z.; Li, X.; Shi, W.; Li, Z.; Guo, Y.; Chen, Q.; Peng, L.; Wei, X. Interlayer Binding Energy of Hexagonal MoS2 as Determined by an In Situ Peeling-to-Fracture Method. *J. Phys. Chem. C* **2020**, *124* (42), 23419−23425.
(30) Weiss, K.; Phillips, J. M. Calculated Specific Surface Energy of Molybdenite (MoS_2). *Phys. Rev. B* **1976**, *14* (12), 5392−5395.
(31) Ferrini, G.; Viggiani, A.; Sertore, D.; Michelato, P.; Parmigiani, F. Linear and Nonlinear Total-Yield Photoemission Observed in the Subpicosecond Regime in Mo. *Phys. Rev. B* **1999**, *60* (11), 8383−8387.
(32) Björkman, T.; Gulans, A.; Krasheninnikov, A. V.; Nieminen, R. M. Van Der Waals Bonding in Layered Compounds from Advanced Density-Functional First-Principles Calculations. *Phys. Rev. Lett.* **2012**, *108* (23), No. 235502.
(33) Vilá, R. A.; Rao, R.; Muratore, C.; Bianco, E.; Robinson, J. A.; Maruyama, B.; Glavin, N. R. In Situ Crystallization Kinetics of Two-Dimensional MoS2. *2D Mater.* **2018**, *5* (1), No. 011009.
(34) Austin, D.; Gliebe, K.; Muratore, C.; Boyer, B.; Fisher, T. S.; Beagle, L. K.; Benton, A.; Look, P.; Moore, D.; Ringe, E.; Treml, B.; Jawaid, A.; Vaia, R.; Joshua Kennedy, W.; Buskohl, P.; Glavin, N. R. Laser Writing of Electronic Circuitry in Thin Film Molybdenum Disulfide: A Transformative Manufacturing Approach. *Mater. Today* **2021**, *43*, 17−26.
(35) McConney, M. E.; Glavin, N. R.; Juhl, A. T.; Check, M. H.; Durstock, M. F.; Voevodin, A. A.; Shelton, T. E.; Bultman, J. E.; Hu, J.; Jespersen, M. L.; Gupta, M. K.; Naguy, R. D.; Colborn, J. G.; Haque, A.; Hagerty, P. T.; Stevenson, R. E.; Muratore, C. Direct Synthesis of Ultra-Thin Large Area Transition Metal Dichalcogenides and Their Heterostructures on Stretchable Polymer Surfaces. *J. Mater. Res.* **2016**, *31* (7), 967−974.
(36) Wieting, T. J.; Verble, J. L. Infrared and Raman Studies of Long-Wavelength Optical Phonons in Hexagonal Mo${\mathrm{S}}_{2}$. *Phys. Rev. B* **1971**, *3* (12), 4286−4292.
(37) Winer, W. O. Molybdenum Disulfide as a Lubricant: A Review of the Fundamental Knowledge. *Wear* **1967**, *10* (6), 422−452.
(38) Jacobs, T.; Lefever, J.; Carpick, R. A Technique for the Experimental Determination of the Length and Strength of Adhesive

Interactions Between Effectively Rigid Materials. *Tribol. Lett.* **2015**, *59*. DOI: 10.1007/s11249-015-0539-9.
(39) Https://Github.Com/Sathwikreddytoom/In-Situ-Experimental-and-Simulation-Study-of-Adhesion-and-Material-Transfer-between-2D-MoS-2-Films.
(40) Kittel, C. *Introduction to Solid State Physics*; John Wiley & sons, inc, 2005.
(41) Rouhani, M.; Hobley, J.; Lin, K.-I.; Hofmann, M.; Yao, Y.-C.; Chang, Y.-H.; Carpick, R. W.; Schall, J. D.; Jeng, Y.-R. High-Temperature Strain-Mediated Oxidation of 2D MoS2. *Mater. Des.* **2023**, *236*, No. 112490.
(42) Reedy, E. D. Contact Mechanics for Coated Spheres That Includes the Transition from Weak to Strong Adhesion. *J. Mater. Res.* **2007**, *22* (9), 2617−2622.
(43) Maugis, D. Adhesion of Spheres: The JKR-DMT Transition Using a Dugdale Model. *J. Colloid Interface Sci.* **1992**, *150* (1), 243−269.
(44) Derjaguin, B. V.; Muller, V. M.; Toporov, Yu. P. Effect of Contact Deformations on the Adhesion of Particles. *J. Colloid Interface Sci.* **1975**, *53* (2), 314−326.
(45) Stewart, J. A.; Spearot, D. E. Atomistic Simulations of Nanoindentation on the Basal Plane of Crystalline Molybdenum Disulfide (MoS2). *Model. Simul. Mater. Sci. Eng.* **2013**, *21* (4), No. 045003.
(46) Vahdat, V.; Ryan, K. E.; Keating, P. L.; Jiang, Y.; Adiga, S. P.; Schall, J. D.; Turner, K. T.; Harrison, J. A.; Carpick, R. W. Atomic-Scale Wear of Amorphous Hydrogenated Carbon during Intermittent Contact: A Combined Study Using Experiment, Simulation, and Theory. *ACS Nano* **2014**, *8* (7), 7027−7040.
(47) Bernal, R. A.; Chen, P.; Schall, J. D.; Harrison, J. A.; Jeng, Y.-R.; Carpick, R. W. Influence of Chemical Bonding on the Variability of Diamond-like Carbon Nanoscale Adhesion. *Carbon* **2018**, *128*, 267−276.
(48) Milne, Z. B.; Schall, J. D.; Jacobs, T. D. B.; Harrison, J. A.; Carpick, R. W. Covalent Bonding and Atomic-Level Plasticity Increase Adhesion in Silicon−Diamond Nanocontacts. *ACS Appl. Mater. Interfaces* **2019**, *11* (43), 40734−40748.
(49) Stukowski, A. Visualization and Analysis of Atomistic Simulation Data with OVITO−the Open Visualization Tool. *Model. Simul. Mater. Sci. Eng.* **2010**, *18* (1), No. 015012.
(50) Buldum, A.; Lu, J. P. Atomic Scale Sliding and Rolling of Carbon Nanotubes. *Phys. Rev. Lett.* **1999**, *83* (24), 5050−5053.
(51) Schall, J. D.; Brenner, D. W. Molecular Simulations of Carbon Nanotube Rolling and Sliding on Graphite. *Mol. Sim.* **2000**, *25* (1−2), 73−79.
(52) Oviedo, J. P.; KC, S.; Lu, N.; Wang, J.; Cho, K.; Wallace, R. M.; Kim, M. J. In Situ TEM Characterization of Shear-Stress-Induced Interlayer Sliding in the Cross Section View of Molybdenum Disulfide. *ACS Nano* **2015**, *9* (2), 1543−1551.
(53) Polfus, J. M.; Muñiz, M. B.; Ali, A.; Barragan-Yani, D. A.; Vullum, P. E.; Sunding, M. F.; Taniguchi, T.; Watanabe, K.; Belle, B. D. Temperature-Dependent Adhesion in van Der Waals Heterostructures. *Adv. Mater. Interfaces* **2021**, *8* (20), No. 2100838.
(54) Wei, Y. A Stochastic Description on the Traction-Separation Law of an Interface with Non-Covalent Bonding. *J. Mech. Phys. Solids* **2014**, *70*, 227−241.
(55) Muratore, C.; Voevodin, A. A. Control of Molybdenum Disulfide Basal Plane Orientation during Coating Growth in Pulsed Magnetron Sputtering Discharges. *Thin Solid Films* **2009**, *517* (19), 5605−5610.
(56) Muratore, C.; Hu, J. J.; Wang, B.; Haque, M. A.; Bultman, J. E.; Jespersen, M. L.; Shamberger, P. J.; McConney, M. E.; Naguy, R. D.; Voevodin, A. A. Continuous Ultra-Thin MoS2 Films Grown by Low-Temperature Physical Vapor Deposition. *Appl. Phys. Lett.* **2014**, *104* (26), No. 261604.
(57) Milne, Z. B.; Bernal, R. A.; Carpick, R. W. Sliding History-Dependent Adhesion of Nanoscale Silicon Contacts Revealed by in Situ Transmission Electron Microscopy. *Langmuir* **2019**, *35* (48), 15628−15638.
(58) Sader, J. E.; Chon, J. W. M.; Mulvaney, P. Calibration of Rectangular Atomic Force Microscope Cantilevers. *Rev. Sci. Instrum.* **1999**, *70* (10), 3967−3969.
(59) Polak, E.; Ribiere, G. Note Sur La Convergence de Méthodes de Directions Conjuguées. *Revue française d'informatique et de recherche opérationnelle. Série rouge* **1969**, *3*, 35−43.
(60) Berendsen, H. J. C.; Postma, J. P. M.; van Gunsteren, W. F.; DiNola, A.; Haak, J. R. Molecular Dynamics with Coupling to an External Bath. *J. Chem. Phys.* **1984**, *81* (8), 3684−3690.
(61) Thompson, A. P.; Aktulga, H. M.; Berger, R.; Bolintineanu, D. S.; Brown, W. M.; Crozier, P. S.; in 't Veld, P. J.; Kohlmeyer, A.; Moore, S. G.; Nguyen, T. D.; Shan, R.; Stevens, M. J.; Tranchida, J.; Trott, C.; Plimpton, S. J. LAMMPS - a Flexible Simulation Tool for Particle-Based Materials Modeling at the Atomic, Meso, and Continuum Scales. *Comput. Phys. Commun.* **2022**, *271*, No. 108171.
(62) Tersoff, J. Chemical Order in Amorphous Silicon Carbide. *Phys. Rev. B* **1994**, *49* (23), 16349−16352.
(63) Liang, T.; Phillpot, S. R.; Sinnott, S. B. Parametrization of a Reactive Many-Body Potential for Mo–S Systems. *Phys. Rev. B* **2009**, *79* (24), No. 245110.
(64) Brenner, D. W.; Shenderova, O. A.; Harrison, J. A.; Stuart, S. J.; Ni, B.; Sinnott, S. B. A Second-Generation Reactive Empirical Bond Order (REBO) Potential Energy Expression for Hydrocarbons. *J. Phys.: Condens. Matter* **2002**, *14* (4), 783.
(65) Jones, J. E.; Chapman, S. On the Determination of Molecular Fields.—I. From the Variation of the Viscosity of a Gas with Temperature. *Proc. R. Soc. London Ser. Contain. Pap. Math. Phys. Character* **1924**, *106* (738), 441−462.
(66) Jones, J. E.; Chapman, S. On the Determination of Molecular Fields. —II. From the Equation of State of a Gas. *Proc. R. Soc. London Ser. Contain. Pap. Math. Phys. Character* **1924**, *106* (738), 463−477.
(67) Jiang, J.-W.; Park, H. S. A Gaussian Treatment for the Friction Issue of Lennard-Jones Potential in Layered Materials: Application to Friction between Graphene, MoS2, and Black Phosphorus. *J. Appl. Phys.* **2015**, *117* (12), No. 124304.
(68) Rappe, A. K.; Casewit, C. J.; Colwell, K. S.; Goddard, W. A. I.; Skiff, W. M. UFF, a Full Periodic Table Force Field for Molecular Mechanics and Molecular Dynamics Simulations. *J. Am. Chem. Soc.* **1992**, *114* (25), 10024−10035.
(69) Loong, C.-K.; Vashishta, P.; Kalia, R. K.; Jin, W.; Degani, M. H.; Hinks, D. G.; Price, D. L.; Jorgensen, J. D.; Dabrowski, B.; Mitchell, A. W.; Richards, D. R.; Zheng, Y. Phonon Density of States and Oxygen-Isotope Effect inBa1−xKxBiO3. *Phys. Rev. B* **1992**, *45* (14), 8052.
(70) Varshney, V.; Patnaik, S. S.; Muratore, C.; Roy, A. K.; Voevodin, A. A.; Farmer, B. L. MD Simulations of Molybdenum Disulphide (MoS2): Force-Field Parameterization and Thermal Transport Behavior. *Comput. Mater. Sci.* **2010**, *48* (1), 101−108.